Full Attitude Control of a VTOL tailsitter UAV

Full Attitude Control of a VTOL Tailsitter UAV

S. Verling[1], B. Weibel[2], M. Boosfeld[2], K. Alexis[3], M. Burri[1], and R. Siegwart[1]

***Abstract*— This paper addresses the challenges of the design, development and control of a new convertible VTOL tailsitter unmanned aerial vehicle that combines the advantages of both fixed wing and rotary wing systems. Wind tunnel measurements are used to get an understanding of the control allocation and to model the static forces and moments acting on the system. Based on the derived model, a novel controller that operates in $\mathcal{SO}(3)$ and handles the dynamics of the vehicle at any attitude configuration, including the rotorcraft and fixed–wing regimes as well as their transitions, is presented. This unified controller allows the autonomous transition of the system without discontinuities of switching, as well as its overall high performance flight control. The capabilities and flying qualities of the platform and the controller are demonstrated and evaluated by means of extensive experimental studies.**

I. Introduction

Aerial robots are at the forefront of robotics research at the time, and have managed to raise great interest within our societies. The recent breakthroughs in the fields of sensing, computing, and actuation allowed the development of small, lightweight and cost–effective aerial robots with advanced capabilities. As a result, a multitude of different Unmanned Aerial Vehicle (UAV) configurations have been proposed and developed towards the goal to address a variety of different application scenarios, from proximity inspection to large area monitoring, surveillance, monitoring or even parcel delivery.

In their majority, UAVs can be roughly classified into two groups, namely rotary–wing and fixed–wing systems. Both these groups have their individual advantages and disadvantages, and are therefore tailored to different application scenarios. In a direct comparison of these two different types of UAV configurations (considering similar sizes), the main advantage of rotary–wing against fixed–wing systems are their superior maneuverability and especially their ability to take off and land vertically which eliminates the need for a runway or flat grounds and allows full operational autonomy. On the other hand, fixed–wing systems are more power–efficient and therefore have much longer endurances and higher operational range. In order to combine the advantages of both vehicle configurations, the UAV presented in this paper, called "Pacflyer S100" and shown in Figure 1, employs a special *VTOL Tailsitter* [1] design and achieves efficient, long–endurance cruise flight like a fixed–wing system while retaining the ability of vertical take off and landing. This combined maneuverability and forward flight efficiency paves the way for increased operational capacity and versatility within a range of possible applications such as inspection of power utilities [2], search and rescue [3], conservation [4], [5] and precision farming [6]–[8]. In such application scenarios, either due to the distributed nature of infrastructure facilities or due to the large rural environments, that furthermore do not provide runaways, the need for long endurance, but also convenient take off and landing on–spot becomes evident.

Fig. 1: The Pacflyer S100 during vertical take off.

However, the unique flight envelope of this aerial robot does pose certain challenges for the problems of modeling and control. To enable the utilization of the complete decision space (selection of flight mode configuration), smooth transition from one flight mode to the other and essentially seamless navigation at any flight configuration becomes necessary. Therefore a control law that handles the full flight envelope has to be developed. This paper addresses the problem of modelling the vehicle dynamics and aerodynamics (with the support of wind tunnel measurements) and proposes a nonlinear control law that operates in $\mathcal{SO}(3)$ and ensures stability and high performance for *any attitude configuration* of the vehicle, handles the transition from vertical to forward flight, and facilitates the autonomous operation of this aerial robot. To evaluate the performance of the controller, extensive experimental studies were conducted dealing with the most challenging subsets of the flight envelope of the Pacflyer S100. It is clarified that the terminology of "Full Attitude Control" in this paper does not include heading.

The remainder of this paper is structured as follows. In Section II, an overview of the system will be presented,

[1] Sebastian Verling, Michael Burri and Roland Siegwart are with the Autonomous Systems Lab, ETH Zurich, Leonhardstrasse 21, 8092 Zurich, Switzerland, sebastian.verling@mavt.ethz.ch

[2] Maximilian Boosfeld and Basil Weibel are with Wingtra, ETH Zurich ieLab LEO, Leonhardstrasse 27, 8092 Zurich, Switzerland

[3] Kostas Alexis is with the University of Nevada, Reno, 1664 N. Virginia Street, Reno, NV, 89557, USA

followed by the modeling of the system in Section III. The control strategy is overviewed in Section IV and experimental verification is presented in Section V. Finally, conclusions are drawn in Section VI.

II. System Overview

This Section presents the newly designed and manufactured aerial robot in more detail. The main design and its components are explained in subsections II-A, II-B and II-C, while the consequential properties and flight behaviour will be illustrated in Subsections II-D and II-F. Subsection II-E deals with the coordinate systems that are used in this paper.

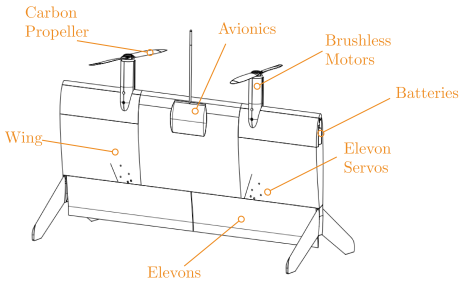

Fig. 2: Hardware configuration of the Pacflyer S100

The system is designed to use a minimum combination of motors and elevons to control the system within its whole flight envelope. Therefore, the proposed design does not require additional hardware for the transition maneuver, as opposed to other design concepts such as tilt rotors [9]–[12]. This allows maintaining a low cost, low complexity system. Figure 2 shows a schematic representation of the Pacflyer S100. As shown, the system consists of one wing with two motors and two elevons. The batteries are integrated into the wing. In the vehicle center, the electronics box containing the Pixhawk autopilot [13] platform with the corresponding avionics is shown. The whole system has a mass $m = 2.5$kg

A. Wing

The wing of the system has a span $S = 1$m and a chord length $c = 0.45$m. The profile of the wing is the PW75 [14], [15] proposed by Peter Wick for wing–only designs such as the presented one. With the presented design, the two elevons as seen in Figure 2, take the whole span of the available wing and have a chord of 30%. These elevons have a range of $\pm 30°$ and are actuated with servos integrated in the wing.

B. Propulsion

For its propulsion the described system uses two carbon propellers with a diameter of 14" which are powered by 900W brushless electrical motors. The propellers cover almost the whole wing surface in order to create enough airflow to control the system during the hover regime (see actuation principle in Subsection II-F). The power supply for each of the motors is a 6s LIPO battery, which is integrated into the sides of the wing, as shown in Figure 2.

Fig. 3: The PW75 airfoil [14], [15]

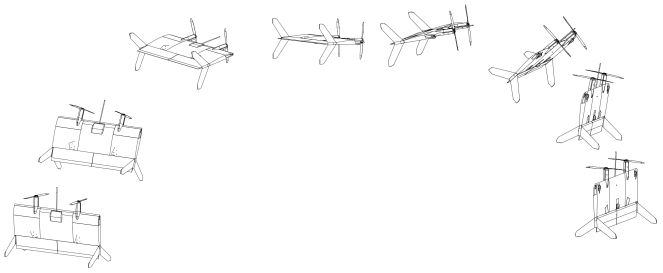

Fig. 4: Illustration of the flight envelope of the Pacflyer S100

C. Avionics

In order to estimate the pose of the vehicle and enable its automatic control, the following sensors were used: An Inertial Measurement Unit (IMU) with integrated 3 axes accelerometer and gyroscope to measure the accelerations and angular velocities that are acting on the system, a magnetometer to measure the magnetic flux, a GPS module for position updates, a barometer to assess the atmospheric pressure and a differential pressure sensor to determine the velocity of the airstream. All the information gathered from the sensors is then fused to estimate the pose using the Extended Kalman Filter (EKF) of the Pixhawk open source software stack [13].

The core of the avionics is the Pixhawk Autopilot [13] incorporating the IMU, the magnetometer, and barometer, as well as a 168MHz Cortex M4F CPU to process the data.

D. Flight Envelope

Figure 4 shows the typical flight envelope of the proposed system. When taking off, the propellers point upwards allowing the system to hover. Subsequently, the transition gets triggered and the whole system pitches $90°$ forward. The lift is now produced by the aerodynamic effects of the wing instead of the propellers. This allows decreasing the power consumption to roughly one fourth. Once the system reaches the desired landing point, it pitches $90°$ upwards and lands on the ground while hovering.

E. Coordinate Frames

The conventions employed for the two coordinate frames are shown in Figure 5. For the earth frame, the North-East-Down (NED) convention has been chosen, where $\boldsymbol{e}_x$ is north, $\boldsymbol{e}_y$ is east, and $\boldsymbol{e}_z$ is down. The body-fixed coordinates are chosen according to an airplane convention - $\boldsymbol{b}_x$ is perpendicular to the propeller plane, $\boldsymbol{b}_y$ goes from the center to the right side (top view) of the wing and $\boldsymbol{b}_z = \boldsymbol{b}_x \times \boldsymbol{b}_y$.

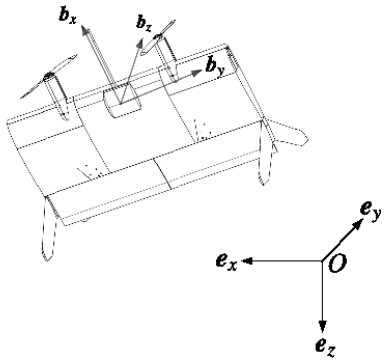

Fig. 5: Illustration of the used coordinate frames

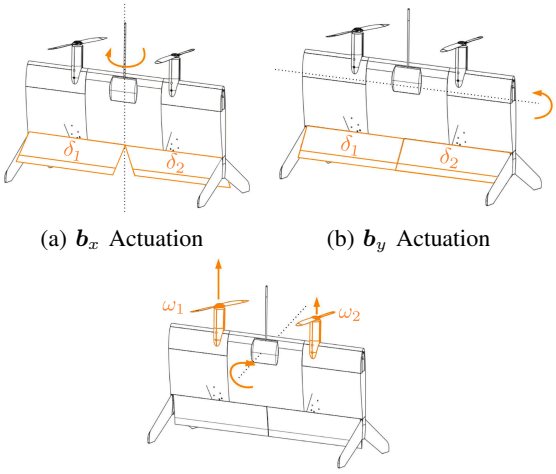

(a) $\boldsymbol{b}_x$ Actuation (b) $\boldsymbol{b}_y$ Actuation

(c) $\boldsymbol{b}_z$ Actuation

Fig. 6: Actuation Principle of the Pacflyer S100

F. Actuation Principle

Given the presented actuation of the system and the negligible coupling between the three body axes, it is a valid simplification to approximate the actuation for each axis independently. The vehicle axis $\boldsymbol{b}_x$ is controlled using the differential elevon deflection as seen in Figure 6a. Axis $\boldsymbol{b}_y$ is similarly steered using equal elevon deflections (Figure 6b). The moments for these two axes are created by diverting the airflow streaming over the wing. This airflow arises from a combination of the propeller slipstream and the velocity $\boldsymbol{v}$ of the system. As the proposed UAV does not have a vertical tail, $\boldsymbol{b}_z$ is controlled by using differential thrust as depicted in Figure 6c.

III. Modeling

The development of a high fidelity model of such a vehicle is a non-trivial process. Yet it corresponds to a necessary step to enable model-based control synthesis and thorough testing and verification prior to flight experiments. To accomplish this task, a methodology that combines rigid-body motion principles [16] and aerodynamics modeling techniques with wind-tunnel data was followed. This section consists of a brief overview of the most important aerodynamic forces that are acting on a wing, followed by the results of the aforementioned wind-tunnel experiments.

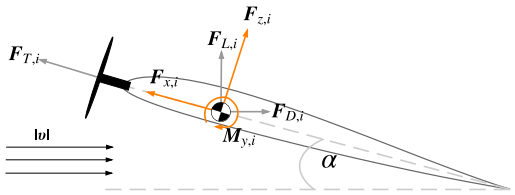

Fig. 7: Aerodynamic forces and moment of one segment (half of the system)

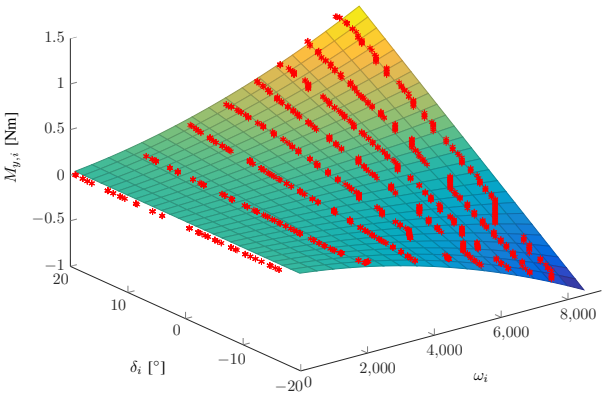

Fig. 8: $M_{y,i}$ of segment i ($|\boldsymbol{v}| = 0\,\mathrm{m\,s^{-1}}$, "hover regime")

A. Aerodynamics

Figure 7 shows the most significant forces that are acting on one segment (half of the UAV) as well as the applied moment. $F_{T,i}$ represents the force created by the propeller i. $F_{L,i}$ and $F_{D,i}$ are the lift and drag forces created by the airfoil of one segment while $M_{y,i}$ is the moment along $\boldsymbol{b}_y$. These forces and moment are then transformed and summarized in the body fixed coordinate system to $F_{x,i}$, $F_{z,i}$ and $M_{y,i}$.

B. Wind-Tunnel Experiment

A force/moment sensor has been attached between the vehicle and the wind-tunnel mounting point. For the wind-tunnel data collection experiments, the angle of attack α, the elevon deflections δ_i, the motor rpm ω_i and the velocity of the wind tunnel $|\boldsymbol{v}|$ have been varied while measuring the forces and moments in all 3 axes of the body.

Figure 8 shows the measurements of $M_{y,i}$ of one wing segment (half of the UAV) from the wind tunnel experiment with zero inflow, i.e. $|\boldsymbol{v}| = 0$, which corresponds to the hover regime of the system. The surface represents the regression surface fitted through the measurements dependent on ω_i and δ_i. The root mean squared error (RMSE) of the fit is $0.065\,\mathrm{N\,m}$. Figure 9 shows the same for a wind tunnel speed $|\boldsymbol{v}| = 16\,\mathrm{m\,s^{-1}}$ and an $\alpha = 5°$ which corresponds to the nominal operating point for cruise flight. Here the RMSE of the fit is $0.057\,\mathrm{N\,m}$. The main characteristics of segment i,

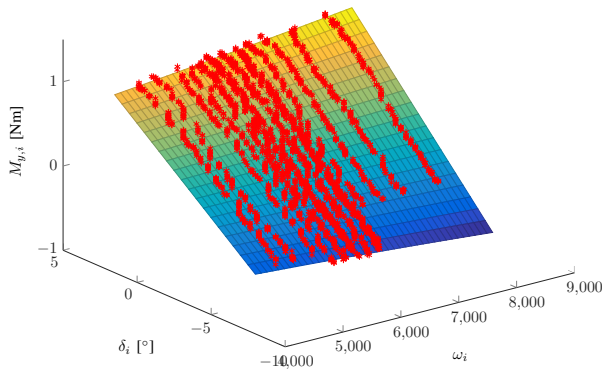

Fig. 9: $M_{y,i}$ of segment i ($|\boldsymbol{v}| = 16\,\mathrm{m\,s^{-1}}$, $\alpha = 5°$, "cruise flight nominal regime")

given $\alpha = 5°$, can be approximated by

$$F_{x,i} = \underbrace{\boldsymbol{c}_{F_{x0}}^{\top} \begin{pmatrix} 1 \\ |\boldsymbol{v}| \\ |\boldsymbol{v}|^2 \end{pmatrix}}_{\mu_i^0(|\boldsymbol{v}|)} + \underbrace{\boldsymbol{c}_{F_{x2}}^{\top} \begin{pmatrix} 1 \\ |\boldsymbol{v}| \end{pmatrix}}_{\mu_i^2(|\boldsymbol{v}|)} \omega_i^2$$

$$M_{y,i} = \underbrace{\boldsymbol{c}_{M_{y0}}^{\top} \begin{pmatrix} 1 \\ \omega_i |\boldsymbol{v}| \end{pmatrix}}_{\eta_i^0(|\boldsymbol{v}|,\omega_i)} + \underbrace{\boldsymbol{c}_{M_{y1}}^{\top} \begin{pmatrix} \omega_i \\ |\boldsymbol{v}|^2 \\ \omega_i^2 \\ \omega_i |\boldsymbol{v}| \end{pmatrix}}_{\eta_i^1(|\boldsymbol{v}|,\omega_i)} \delta_i$$

$$F_{z,i} = \underbrace{\boldsymbol{c}_{F_{z0}}^{\top} \begin{pmatrix} 1 \\ |\boldsymbol{v}|^2 \\ \omega_i^2 \\ \omega_i \\ \omega_i |\boldsymbol{v}| \end{pmatrix}}_{\zeta_i^0(|\boldsymbol{v}|,\omega_i)} + \underbrace{\boldsymbol{c}_{F_{z1}}^{\top} \begin{pmatrix} \omega_i \\ |\boldsymbol{v}|^2 \\ \omega_i^2 \\ \omega_i |\boldsymbol{v}| \end{pmatrix}}_{\zeta_i^1(|\boldsymbol{v}|,\omega_i)} \delta_i \tag{1}$$

with $\boldsymbol{c}_{F_{x0}}$, $\boldsymbol{c}_{F_{x2}}$, $\boldsymbol{c}_{M_{y0}}$, $\boldsymbol{c}_{M_{y1}}$, $\boldsymbol{c}_{F_{z0}}$ and $\boldsymbol{c}_{F_{z1}}$ being constant column vectors estimated from the wind–tunnel data. This model is based on [17] and has been extended to take effects of the propeller slipstream into account. The total forces and moments that are acting on the system are approximated as follows

$$\begin{aligned} F_x &= F_{x,1} + F_{x,2} \\ F_z &= F_{z,1} + F_{z,2} \\ M_x &= l_m (F_{z,1} - F_{z,2}) \\ M_y &= M_{y,1} + M_{y,2} \\ M_z &= l_m (F_{x,1} - F_{x,2}) \end{aligned} \tag{2}$$

where l_m describes the distance along $\boldsymbol{b}_y$ from the middle of one segment (where also the motors are attached to the wing) to the center of gravity of the vehicle. F_x, F_z, M_x, M_y, M_z express the summarized effect of all aerodynamic forces and moments, as described in Subsection III-A, while it is assumed that no other forces or moments are acting on the system.

Given the forces and moments acting on the system, the subsequent step in order to develop the dynamic model of the vehicle is a rigid body representation which can be written as

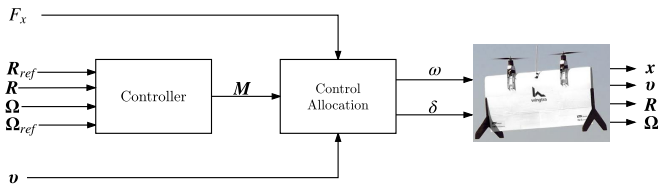

Fig. 10: The control structure of the proposed controller

$$\begin{aligned} \dot{\boldsymbol{x}} &= \boldsymbol{v} \\ m\dot{\boldsymbol{v}} &= m\boldsymbol{g} + \boldsymbol{R}\boldsymbol{F} \\ \dot{\boldsymbol{R}} &= \boldsymbol{R} \times \boldsymbol{\Omega} \\ \boldsymbol{J}\dot{\boldsymbol{\Omega}} &= \boldsymbol{M} - \boldsymbol{\Omega} \times \boldsymbol{J}\boldsymbol{\Omega} \end{aligned} \tag{3}$$

where $\boldsymbol{F} = (F_x, 0, F_z)^{\top}$ and $\boldsymbol{M} = (M_x, M_y, M_z)^{\top}$. $\boldsymbol{x}$ and $\boldsymbol{v}$ describe the position and velocity in the earth coordinates, $\boldsymbol{g}$ describes the gravitational vector and $\boldsymbol{R}$ describes the current rotation from the body frame to the earth frame, $\boldsymbol{\Omega}$ specifies the angular velocity with respect to the body fixed frame, while $\boldsymbol{J}$ is the moment of inertia.

IV. Controller Synthesis

The main structure of the controller is shown in Figure 10 where the first block is the error function that maps the desired attitude and angular rates as well as the actual attitude and angular rates to an artificial control moment as explained in Subsection IV-A. The second block is explained in Subsection IV-B and consists of the mapping from the desired control moments $\boldsymbol{M}$ and force F_x to the actual actuator outputs.

A. Controller

In order to control the proposed system within all its flight regimes, a coordinate-free representation of the attitude is desired. This is why the error function for the proposed controller works in $\mathcal{SO}(3)$ [18], [19] in the interest of avoiding singularities.

In order to guarantee a smooth transition, the controller should work for every attitude configuration, namely in hover, cruise flight and within the transition. This allows having one unified controller without switching between different control loops which could cause non-smooth actuator signals and lead to undesired switching dynamics [20] for each mode of the system. Another desired property of the controller would be an error function that is independent of the heading. One problem when handling the full attitude all at once is that the control moments the vehicle may employ can be rather limited, especially during hover. As explained in Section II-F, the moments along $\boldsymbol{b}_x$ and $\boldsymbol{b}_y$ are both created by using the elevons. Therefore when creating a moment in $\boldsymbol{b}_x$ the system automatically has limited maximum deployable control moments along $\boldsymbol{b}_y$. Accordingly, prioritizing the roll and pitch axes could increase the robustness of the system, as these two axes are the ones responsible for the stability of the system. This would allow a hierarchical control approach that first controls

(a) Behaviour for increasing pitch offset

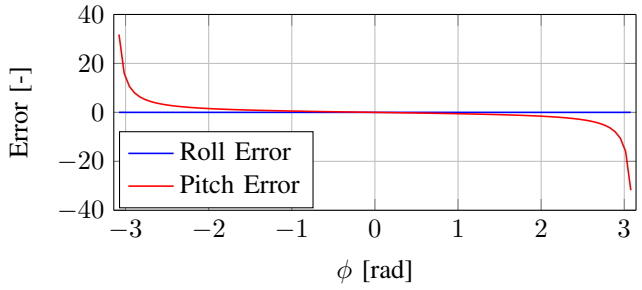

(b) Behaviour for constant pitch offset and varying heading

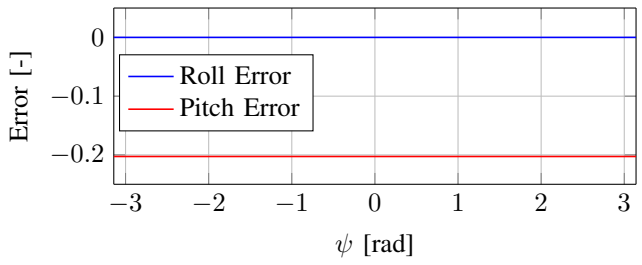

Fig. 11: Error Function Properties. The angles in this Figure correspond to the nominal cruise flight mode of the UAV.

these critical axes and in a subsequent step, when the system is close to its reference, controls the heading. This allows a more robust operation of the system under disturbances, such as wind. This independence of the roll and pitch error with respect to the heading also satisfies the requirement of intuition during tuning, analysis of the data or teleoperation. For even more intuitive tuning, robustly predictable behavior and better responses under large deviations from the setpoint, it is favorable to have a monotonic error function. Based on these desired properties, the following error function for the controller is proposed

$$\begin{aligned} \boldsymbol{M} &= -\boldsymbol{k}_R \boldsymbol{e}_R - \boldsymbol{k}_\omega \boldsymbol{e}_\Omega + \boldsymbol{\Omega}(\boldsymbol{J} \times \boldsymbol{\Omega}) \\ \boldsymbol{e}_R &= \boldsymbol{R}^\top \left(\frac{-\boldsymbol{e}_z \times \boldsymbol{\tau}}{1 - \boldsymbol{e}_z \boldsymbol{\tau}}\right) \\ \boldsymbol{\tau} &= \boldsymbol{R}\boldsymbol{R}_{ref}^T(-\boldsymbol{e}_z) \\ \boldsymbol{e}_\Omega &= \boldsymbol{\Omega} - \boldsymbol{\Omega}_{ref} \end{aligned} \tag{4}$$

with $\boldsymbol{k}_R$ and $\boldsymbol{k}_\Omega$ being diagonal gain matrices for the attitude error and the rate error respectively, while $\boldsymbol{R}_{ref}$ and $\boldsymbol{\Omega}_{ref}$ are the reference for the angle and the angular velocity. Figure 11 shows the error $\boldsymbol{e}_R$ for the roll and pitch axis. It can be seen that it fulfills the desired requirements, i.e. the monotonic behaviour in Figure 11a and the independence of the orientation/heading in Figure 11b.

B. Control Allocation

As described in Section III, the moments and forces acting on the system are not only influenced by the actuators, but also from the current state of the system, i.e. the velocity $\boldsymbol{v}$ of the system and its angle of attack α. Therefore, a state-based control allocation has to be employed in order to create the desired moments. To do so, the equations (1) and (2) (derived in Section III) that map the actuator signals and the state to the moments and forces that are acting on the system are inverted to calculate the needed actuator signals, given the state and desired moments and forces. The resulting actuator outputs are as follows

$$\begin{aligned} F_{x,1} &= \frac{1}{2}(F_x + \frac{M_z}{l_m}) \\ F_{x,2} &= F_x - F_{x,1} \end{aligned} \tag{5}$$

$$\begin{aligned} \omega_i &= \sqrt{\frac{F_{x,i} - \mu_0(|\boldsymbol{v}|)}{\mu_2(|\boldsymbol{v}|)}} \\ \delta_1 &= \frac{-l_m \zeta_2^1(-M_y + \eta_1^0 + \eta_2^0) + \eta_2^1(M_x - \zeta_1^0 l_m + \zeta_2^0 l_m)}{l_m(\zeta_1^1 \eta_2^1 + \zeta_2^1 \eta_1^1)} \\ \delta_2 &= -\frac{l_m \zeta_1^1(-M_y + \eta_1^0 + \eta_2^0) + \eta_1^1(M_x - \zeta_1^0 l_m + \zeta_2^0 l_m)}{l_m(\zeta_1^1 \eta_2^1 + \zeta_2^1 \eta_1^1)} \end{aligned} \tag{6}$$

with ω_1, ω_2, δ_1, and δ_2 being the rpm and elevon deflections respectively of the first and second segment of the UAV, and M_x, M_y, M_z being the commanded moments by the controller, and F_x being the force commanded by a high level controller, e.g. position trajectory control loop or a pilot.

V. Experimental Verification

The controller presented in Section IV has been implemented on the Pixhawk autopilot and integrated to the system. The controller was preliminarily tested with the model. In a subsequent step the system was attached to a test rig that only allowed one axis to move at a time. Using this setup, rough tuning of the gains was possible. Finally progressive testing in the field could be performed, which then allowed fine tuning of the attitude gains. Having the attitude loop fine–tuned, a $\mathcal{L}1$ [21] guidance for fixed wing navigation was also implemented to further demonstrate the capabilities of the overall closed-loop system.

A. Hover Flight

The experimental results of the attitude controller for the pitch and roll axes in hover flight are presented in Figures 12 and 13. In order to avoid the singularity of Euler angles in the plots, the coordinate system has been rotated by 90° along the pitch axis. This is illustrated in the plots by using $\tilde{\phi}$ and $\tilde{\theta}$ for this turned coordinate system. Therefore, "Pitch in hover" $\tilde{\theta}$ and "Roll in hover" $\tilde{\phi}$ correspond to the angles around the nominal hover situation. The plots show that the controller not only stabilizes the system but also provides high quality tracking behaviour for most of its effective bandwidth.

B. Cruise flight

Figures 14 and Figures 15 show the results for the pitch and roll axis during cruise flight. Here "pitch in cruise flight" θ and "roll in cruise flight" ϕ correspond to the angles around nominal cruise flight. As shown, a similar behavior as for hover is observed. Both axes are stabilized and yield good tracking behaviour. The frequency analysis shows that the reference frequencies are tracked over a broad spectrum of frequencies, i.e. up to $20\,\mathrm{rad\,s^{-1}}$ for pitch and $6\,\mathrm{rad\,s^{-1}}$ for roll. This makes sense with respect to the big difference in inertia around the two axes.

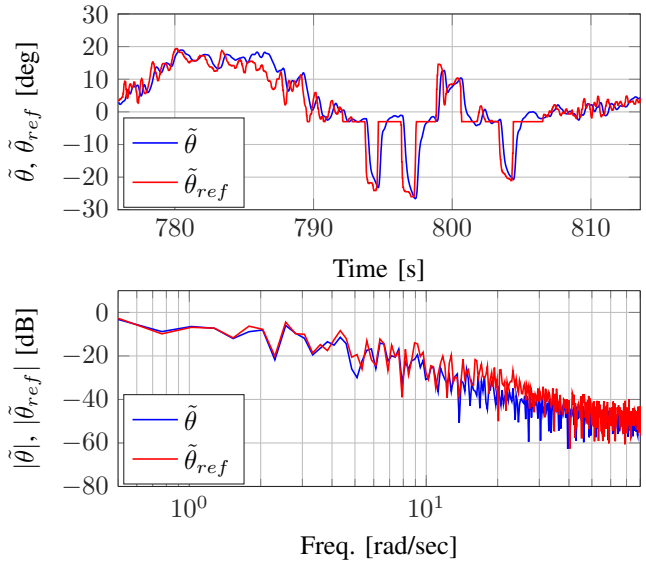

Fig. 12: "Pitch in hover" flight. The term "pitch in hover" refers to a pitch angle measured around the hover flight mode of the UAV

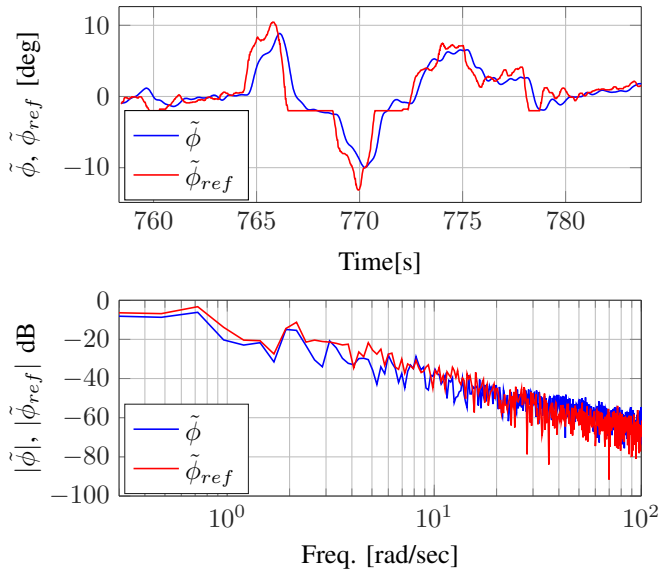

Fig. 13: "Roll in hover" flight. The term "roll in hover" refers to a roll angle measured around the hover flight mode of the UAV

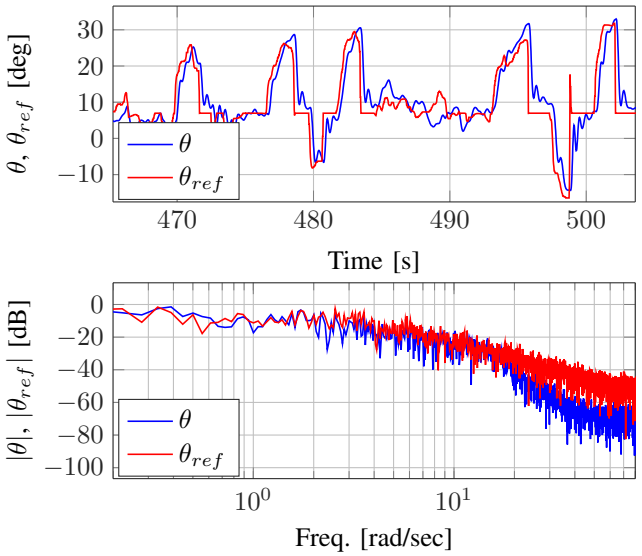

Fig. 14: Analysis of "pitch in cruise". The term "pitch in cruise" refers to a pitch angle measured around the cruise flight mode of the UAV.

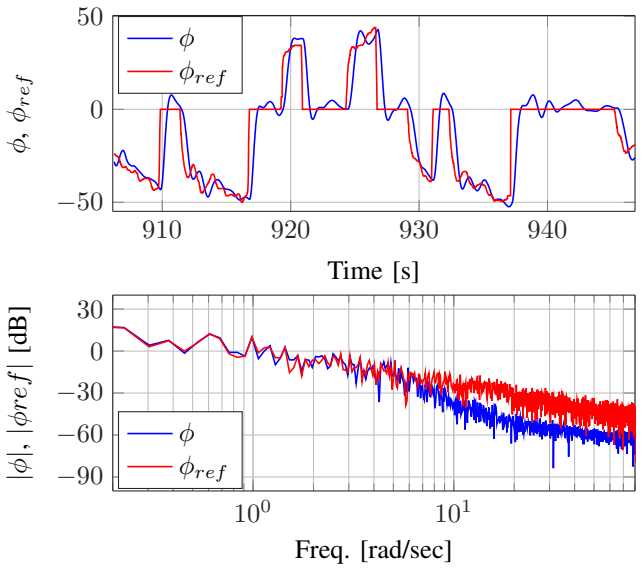

Fig. 15: Analysis of "roll in cruise". The term "roll in cruise" refers to a roll angle measured around the cruise flight mode of the UAV.

C. Transition

The transition from hover to cruise and vice versa are depicted in Figures 16 and 17 respectively. Here again the pitching angle θ corresponds to the angle in nominal cruise flight. As soon as the transition gets triggered, a constant pitch rate reference Ω_{ref_y}, and a linear rising reference angle θ_{ref} are fed into the controller until θ_{ref} reaches its final value. This phase is illustrated with the grey background in both of the figures and lasts for 1.5s. One can see that the transition from hover to cruise is smooth and follows the reference with a time lag of less than 0.5s. The transition back from cruise to hover needs more time to finish and yields slight oscillations. This can be explained by the sudden increase of the angle of attack α and the resulting nonlinear aerodynamic effects.

Overall, the closed-loop system yields good attitude tracking behaviour within both rotorcraft and fixed-wing flight regime, as well as during the transition.

D. $\mathcal{L}1$ Navigation

After having the attitude control loop working in all flight regimes of the vehicle, a high level navigation loop was implemented to close the guidance loop in the cruise flight mode and further demonstrate the capabilities of the platform. The guidance approach is the $\mathcal{L}1$ navigation [21]

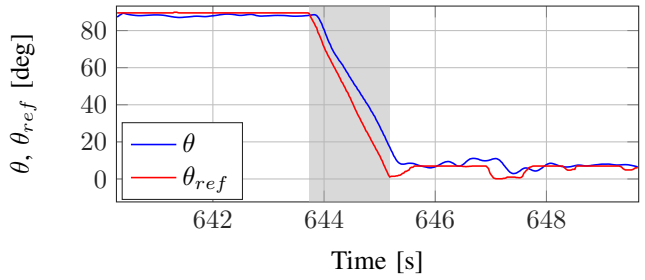

Fig. 16: Transition from hover to cruise. The angle θ refers to the pitch angle in cruise flight mode of the UAV.

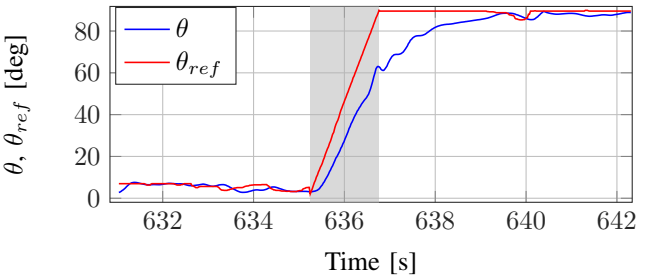

Fig. 17: Transition from cruise to hover. The angle θ refers to the pitch angle in cruise flight mode of the UAV.

and the results are shown in Figure 18. It shows the system flying to a specified waypoint and loiter subsequently around it with a loiter radius $r_L = 50$m.

VI. Conclusion and Future Work

A new system merging both the advantages of fixed wing systems and rotary wing ones is presented. For that system, a high fidelity model based on wind tunnel data is derived. A new controller functioning in $\mathcal{SO}(3)$ is proposed which can handle any possible attitude configuration of the system. The error function works independent of heading and therefore enables a hierarchical control approach. Extensive tests on the real system confirmed this new proposed controller to yield good results. Stable transition dynamics were achieved, while the transition from cruise flight to hover seems to be more affected by nonlinear effects. The next steps are to improve this transition by means of a model-based optimal transition trajectory, and advancing the guidance law for both cruise and hover flight regimes. Current and future work also addresses the challenge of flying subject to significant wind disturbances to further robustify the take off and landing maneuvers of the vehicle.

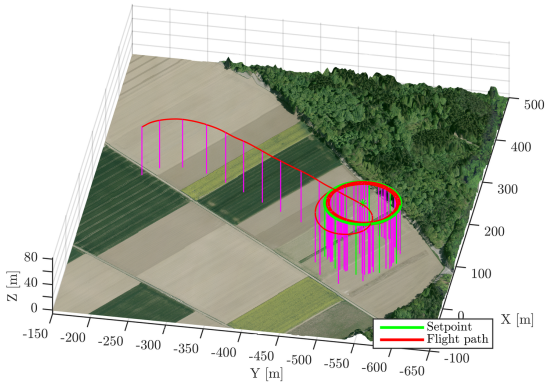

Fig. 18: $\mathcal{L}1$ navigation demonstration. ENU coordinates are used to plot the results on top of the textured, digital elevation map of the environment.

Acknowledgment

The authors would like to thank the whole Wingtra Team for their great support during the testing of the platform.

References

[1] D. Kubo, "Study on design and transitional flight of tail-sitting VTOL UAV," *Proceedings of 25th Congress of ICAS*, 2006.

[2] S. Montambault, J. Beaudry, K. Toussaint, and N. Pouliot, "On the application of VTOL UAVs to the inspection of power utility assets," *2010 1st International Conference on Applied Robotics for the Power Industry, CARPI 2010*, 2010.

[3] M. Bernard, K. Kondak, I. Maza, and A. Ollero, "Autonomous transportation and deployment with aerial robots for search and rescue missions," *Journal of Field Robotics*, vol. 28, no. 6, pp. 914–931, 2011.

[4] L. P. Koh and S. A. Wich, "Dawn of drone ecology : low-cost autonomous aerial vehicles for conservation," *Tropical Conservation Science*, vol. 5, no. 2, pp. 121–132, 2012.

[5] A. Muccio and T. Scruggs, "Moving Target Indicator (MTI) applications for Unmanned Aerial Vehicles (UAVS)," *2003 Proceedings of the International Conference on Radar (IEEE Cat. No.03EX695)*, pp. 541–546, 2003.

[6] W. Bingfang, M. Jihua, Z. Feifei, D. Xin, Z. Miao, and C. Xueyang, "Applying remote sensing in precision farming-a case study in Yucheng," *World Automation Congress (WAC), 2010*, vol. 86, no. 10, pp. 1–6, 2010.

[7] T. Selige and U. Schmidhalter, "Soil Resource Mapping for Precision Farming Using Remote Sensing," vol. 00, no. C, pp. 7031–7033, 2001.

[8] R. Sugiura, T. Fukagawa, N. Noguchi, K. Ishii, Y. Shibata, and K. Toriyama, "Field information system using an agricultural helicopter towards precision farming," *Proceedings 2003 IEEE/ASME International Conference on Advanced Intelligent Mechatronics (AIM 2003)*, vol. 2, no. Aim, pp. 1073–1078, 2003.

[9] G. Notarstefano and J. Hauser, "Modeling and dynamic exploration of a Tilt-Rotor VTOL aircraft," *IFAC Proceedings Volumes (IFAC-PapersOnline)*, no. August 2015, pp. 119–124, 2010.

[10] G. R. Flores-Colunga and R. Lozano-Leal, "A nonlinear control law for hover to level flight for the quad tilt-rotor uav," 2014.

[11] G. Di Francesco and M. Mattei, "Modeling and incremental nonlinear dynamic inversion control of a novel unmanned tiltrotor," *Journal of Aircraft*, pp. 1–14, 2015.

[12] C. Papachristos, K. Alexis, and A. Tzes, "Dual–authority thrust–vectoring of a tri–tiltrotor employing model predictive control," *Journal of Intelligent & Robotic Systems*, pp. 1–34, 2015.

[13] "Pixhawk Autopilot Research Project." https://pixhawk.org.

[14] P. Wick, "Peter Wicks Airfoils for Plank Planforms," *Radio Controlled Soaring Digest*, vol. 22, pp. 39–44, 2005.

[15] P. Wick, "Peter Wick on Planks," *Radio Controlled Soaring Digest*, vol. 23, pp. 28–33, 2006.

[16] D. T. Greenwood, *Principles of dynamics*, vol. 279. 1965.

[17] J. D. Anderson, *Fundamentals of Aerodynamics*, vol. 1984 of *McGraw-Hill Series in Aeronautical and Aerospace Engineering*. McGraw-Hill, 2007.

[18] T. Lee, M. Leok, and N. H. Mcclamroch, "Geometric Tracking Control of a Quadrotor UAV on SE (3)," *Control*, vol. math.OC, no. 3, pp. 5420–5425, 2010.

[19] S. D. Cairano, "Constrained Spacecraft Attitude Control on SO (3) Using Reference Governors and Nonlinear Model Predictive Control," no. 3, 2014.

[20] D. Liberzon *et al.*, "Basic problems in stability and design of switched systems," *Control Systems, IEEE*, vol. 19, no. 5, pp. 59–70, 1999.

[21] S. Park, J. Deyst, and J. How, "A New Nonlinear Guidance Logic for Trajectory Tracking," *AIAA Guidance, Navigation, and Control Conference and Exhibit*, pp. 1–16, Aug. 2004.